

# Tunable Wettability with Stretchable Microstructured Surfaces

Hoang Huy Vu, Nam-Trung Nguyen,\* Nhat-Khuong Nguyen, Cuong Hung Luu, Samith Hettiarachchi, and Navid Kashaninejad\*

Analyzing the wettability of stretchable microstructured surfaces is crucial in applications like soft robotics, wearable biosensors, stretchable electronics, and electronic skin (e-skin). However, it remains unclear how stretching affects the surface free energy (SFE) of these stretchable surfaces. In this article, stretchable microstructured surfaces are designed and fabricated, enabling liquid droplets to stay on top of the surface gaps. The corresponding SFE values are quantified as a function of both micropillar geometry and strain. It is observed that stretching could significantly affect their SFE and wettability. For instance, for the microstructured surface with pillar and gap dimensions of 10  $\mu\text{m}$ , increasing the strain from 0% to 50% causes a sevenfold increase in the effective SFE. Interestingly, reversible decreasing of the strain decreases SFE to its original value, suggesting that the SFE remains unchanged after a complete stretching and releasing cycle. This trend agrees with the measurement of apparent contact angle (CA) as a function of strain. The results demonstrate stretching's capacity to significantly increase the wettability of microstructured surfaces, leading to a decrease in the CA and an increase in SFE. These findings further shed light on understanding the tunable wettability of microstructured surfaces under various deformation conditions.

microfluidics, drag reduction, and self-cleaning surfaces.<sup>[2]</sup> The design of microstructured surfaces with specific wetting properties depends on the shape and size of the microstructures.<sup>[3]</sup>

The wettability of micropatterned surface can also be adjusted by employing diverse pillar shapes. If pillars are organized in a square array, the wetting characteristics exhibit uniformity across all directions on these surfaces.<sup>[4]</sup> This arrangement causes the sessile droplet to adopt an almost spherical shape, resulting in a consistent apparent contact angle (CA) across the micropatterned surface. Consequently, it is appropriate to refer to this as an isotropic surface structure, or more precisely, a quasi-isotropic surface structure. Conversely, when a material's surface structure exhibits variations depending on different orientations, it is termed an anisotropic surface structure. Jokinen et al. demonstrated

the asymmetrical shape of triangles, promoting controlled directional wetting.<sup>[5]</sup>

The wetting property of surface is commonly understood to be controlled by the chemical composition and physical structure of the surface.<sup>[6]</sup> The factors influencing and tuning the wettability of micropatterned surfaces are chemical modification,<sup>[7]</sup> light illumination,<sup>[7,8]</sup> temperature,<sup>[9]</sup> pressure, plasma treatment,<sup>[10,11]</sup> vibration or oscillation,<sup>[12]</sup> and electromagnetic field.<sup>[13]</sup> Liu et al. utilized a fast and straightforward method for selectively tuning the wettability of a microfluidic device using localized corona discharge.<sup>[14]</sup> This method effectively turned the surface area hydrophilic for generating double emulsions.


Recently, there has been a growing interest in developing stretchable microstructured surfaces for studying surface wettability.<sup>[15,16]</sup> These surfaces may undergo mechanical deformation while still maintaining their surface properties, making them ideal for exploring the effect of surface topography on wettability. Most importantly, stretchable microstructured surfaces potentially contribute significantly to the emerging fields of micro elastofluidics,<sup>[17]</sup> stretchable electronics,<sup>[18]</sup> e-skin,<sup>[19]</sup> wearable microneedles,<sup>[20]</sup> and on-skin wearable systems.<sup>[21]</sup> Stretchable microstructured surfaces have been used to develop soft sensors attached to the skin to monitor various physiological signals such as temperature, pressure, and humidity. These sensors can monitor patients with chronic illnesses or track

## 1. Introduction

Microstructured surfaces have drawn significant attention from the research community due to their unique properties, such as high surface area, low adhesion, and high hydrophobicity.<sup>[1]</sup> The wetting properties of such surfaces are of great importance in many applications, including biomedical devices,

H. H. Vu, N.-T. Nguyen, N.-K. Nguyen, C. H. Luu, S. Hettiarachchi, N. Kashaninejad  
Queensland Micro- and Nanotechnology Centre  
Nathan Campus  
Griffith University  
170 Kessels Road, Brisbane, QLD 4111, Australia  
E-mail: nam-trung.nguyen@griffith.edu.au;  
n.kashaninejad@griffith.edu.au

C. H. Luu  
School of Environment and Science  
Griffith University  
Nathan, QLD 4111, Australia

 The ORCID identification number(s) for the author(s) of this article can be found under <https://doi.org/10.1002/adem.202300821>.

© 2023 The Authors. Advanced Engineering Materials published by Wiley-VCH GmbH. This is an open access article under the terms of the Creative Commons Attribution-NonCommercial License, which permits use, distribution and reproduction in any medium, provided the original work is properly cited and is not used for commercial purposes.

DOI: 10.1002/adem.202300821

athletes' health status. As such, fundamental understanding of wettability of these surfaces is of paramount importance.

Whyman et al. initially explored the influence of stretching on the surface energy and wettability of polymeric surfaces.<sup>[10]</sup> The apparent CA showed no variation between plasma-untreated inflated and deflated polyisoprene latex balloons. The apparent CAs of inflatable balloons were unaffected by their stretching during inflation, but they exhibited sensitivity to plasma treatment. Following a plasma treatment, the latex balloons showed a lower apparent CA before inflation than the untreated ones. The deflation of plasma-treated latex balloons led to a significant rise in surface charge density, causing complete wetting on the surface. Zhang et al. demonstrated that mechanical stretching could significantly improve the water CA of poly(tetrafluoroethylene) (PTFE) films.<sup>[22]</sup> Later, the same group reported the reversible transition wettability states of an elastic polyamide film with a triangular net-like structure by extending and unloading the film.<sup>[23]</sup> Lin et al. fabricated wrinkled polydimethylsiloxane (PDMS) structures with dual-scale roughness by coating silica nanoparticles on the wrinkled PDMS films.<sup>[24]</sup> By quantifying the water CAs on these surfaces, the team showed that the wettability of these surfaces could be tuned by applying a mechanical strain. Notably, the dual-scale roughness was found to be responsible for the wetting transition from complete wetting (Wenzel state) to nonwetting (Fakir Cassie state) condition. Subsequently, Lee et al. investigated the dynamic wetting behavior of hydrophobic PDMS substrates with hierarchical wrinkles by quantifying droplet impacts on these surfaces under 100% stretching.<sup>[25]</sup> Coux et al. used a highly elastic polymer, vinyl polysiloxane (VPS), to fabricate highly stretchable micropillar surfaces.<sup>[15]</sup> The team characterized the wettability of these surfaces by measuring the apparent CAs, CA hysteresis, and contact radius of water droplets under both uniaxial and biaxial extensions. Recently, Liu et al. investigated the wettability of micropatterned surfaces using a shape memory polymer, poly(ethylene-co-vinyl acetate) (EVA).<sup>[26]</sup> The group fabricated three types of EVA-based micropatterned surfaces, namely microcubes, microgrooves, and micropillars. Using a standard static tensile testing machine, the EVA-based micropatterned surfaces were stretched and recovered. Accordingly, the wettability of the micropatterned surfaces was investigated by measuring the apparent water CA and rolling angles under the three states of nonstretched (initial), stretched, and recovered conditions.

On the other hand, it is well known that wetting conditions highly depend on the type of liquid used for CA measurements. For example, most superhydrophobic surfaces (with a water CA over 150°) have an oil CA of less than 10°.<sup>[27]</sup> As such, to better quantify the wettability of a surface, its corresponding surface-free energy (SFE) should also be quantified. Moreover, SFE plays a vital role in determining the interaction between a solid surface and biological fluids and cells.<sup>[28]</sup> However, methods for calculating the SFE of solids assumed that the surface is atomically smooth and homogenous. To take the effect of roughness into account, Biolin Scientific® developed an optical tensiometer with a 3D topography module that can measure the SFE of rough surfaces.<sup>[29]</sup> Nevertheless, the system assumes that the wetting condition is Wenzel state, i.e., liquid droplets penetrate entirely into the cavities, as it is thermodynamically the most stable wetting condition. However, the module cannot be used in the case

of hydrophobic micropillar surfaces where liquid droplets stay on top of the pillars, i.e., Fakir Cassie state. Accordingly, normalized surface free energy (NSFE) can represent the wettability of the surface.<sup>[30]</sup>

To the best of our knowledge, the effect of continuous stretching and releasing on the NSFE of hydrophobic micropillar surfaces and its correlation with apparent CAs have not been investigated in the literature; thus, it is the main focus of our present study. To this aim, various PDMS-based micropillar surfaces are fabricated, and the wettability of these surfaces is characterized by measuring both NSFE and apparent CAs. Accordingly, NSFE values are first discussed as a function of the gap and the diameter of the PDMS micropillars. The results are subsequently compared to the SFE of flat PDMS. Furthermore, we investigate the effects of systematic stretching and releasing on the variation of NSFE values and apparent CAs.

The findings of the present study will provide valuable insights into the behavior of stretchable microstructured surfaces with tunable wettability and their interaction with aqueous solutions, biological fluids, and other liquids.

## 2. Experimental Section

### 2.1. Fabrication of the Mould

Figure 1 illustrates the fabrication process of micropillars with identical circular shape, diameters ( $L$ ), gaps ( $G$ ), and height ( $H = 10\ \mu\text{m}$ ) using the conventional soft lithography technique. To start with, a 4-inch silicon (Si) wafer was coated with hexamethyldisilazane (HMDS) (Sigma-Aldrich, Australia) for 30 min prior to resist coating to promote photoresist adhesion. Next, the wafer was spin-coated with a positive photoresist layer (AZ 10XT, MicroChemicals GmbH, Germany). The spinning speed determined the thickness of the coating. After spin coating, the wafer was baked at 100 °C for 3 min to remove excess solvent and improve the adhesion of the photoresist on the wafer. Subsequently, we used a maskless aligner with a 405 nm wavelength (MLA150 Maskless Aligner Heidelberg Instruments, Germany) to expose the patterns directly for about 20 min at an intensity of  $1000\ \text{mJ cm}^{-2}$ . After the development, the exposed photoresist was removed, and different designs of adjacent holes were formed on the 4-inch wafer. The wafer was then rinsed with DI water and dried slowly using nitrogen gas. A mixture of poly(dimethylsiloxane) (PDMS) (Sylgard 184, Dow Corning) and the curing agent with a ratio of 10:1 was poured on the mould. The PDMS layers were cured in an oven for 2 h at 70 °C and then peeled off the wafer. As a result, adjacent pillar arrays were obtained on the surface of the PDMS. Micropillars with a high aspect ratio (height-to-diameter ratio of more than 8) fabricated using photolithography are extremely fragile and can collapse easily.<sup>[31]</sup> The diameters of the pillar ( $L$ ) are 5, 10, 15, and 20  $\mu\text{m}$ , the gaps between neighboring pillars ( $G$ ) are 5, 10, 15, and 20  $\mu\text{m}$ , and the nominal height of the pillar is about 10  $\mu\text{m}$ . The largest aspect ratio is only 2, which is sufficient for the stability of the pillars. The smallest feature of 5  $\mu\text{m}$  can be achievable with the photolithographic resolution of the MLA150 machine.

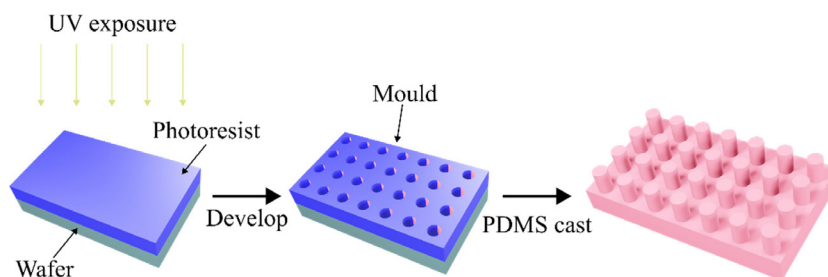


**Figure 1.** Fabrication process of the microstructured PDMS. A clean wafer was spin-coated with a positive photoresist AZ10XT. Then, exposure with a maskless aligner at 405 nm wavelength. With the circular micro-hole arrays standing on the wafer, PDMS was carefully poured onto the mould and then gently peeled from the mould. The PDMS sample with micropillar arrays on the surface is fabricated.

## 2.2. Fabrication of the Stretchable Platform

We designed and fabricated a stretching device, as shown in **Figure 2**. The stretching device consists of a precision positioner mounted on a poly(methyl methacrylate) (PMMA) stage. Two PMMA plates were fitted onto two metal clamps screwed tightly to the stage. The shape of the device was optimized to minimize the fluctuation of the stage during measurement and not to obscure the camera view.

## 2.3. Contact Angle Measurement

Wetting behavior, the way a surface interacts with a liquid, can be determined by the CA. We measured the apparent CAs using an optical tensiometer (Theta Flex, Biolin Scientific, Finland). The CAs were measured in a single viewing direction, as illustrated in

Figure 2a. To ensure that surface tension dominated over gravity and the droplet maintained a spherical shape, a droplet volume of  $\approx 5 \mu\text{L}$  was used. The Bond number ( $Bo$ ) is the ratio between gravity and surface tension.<sup>[32]</sup> Bond number is defined as  $Bo = \frac{(\rho_w - \rho_a)gr^2}{\gamma}$ , where  $\rho_w$  and  $\rho_a$  are densities of water and air,  $g$  is the gravitational acceleration,  $r$  is the radius of the drop, and  $\gamma$  is the surface tension of the liquid.<sup>[33]</sup> Assuming the typical values  $\theta = 90^\circ$ , the droplet volume of  $V = 5 \times 10^{-9} \text{ m}^3$ ,  $\rho_w = 1000 \text{ kg m}^{-3}$ ,  $\rho_a = 1.293 \text{ kg m}^{-3}$ ,  $g = 9.8 \text{ N kg}^{-1}$ ,  $\gamma = 72 \times 10^{-3} \text{ N m}^{-1}$ ,  $r = \frac{3V\sin^3\theta}{\pi(2-3\cos\theta+\cos^3\theta)} = 0.001$ ,<sup>[34]</sup> the Bond number  $Bo = 0.24 < 1$  indicates that gravity's effect on the droplet was negligible.<sup>[35]</sup>

The apparent CA of each sample was determined by carefully placing a small volume of DI water ( $V \approx 5 \mu\text{L}$ ) onto the surface and allowing the droplet to stabilize before capturing and analyzing its image using Thetaflex Optical Tensiometer.

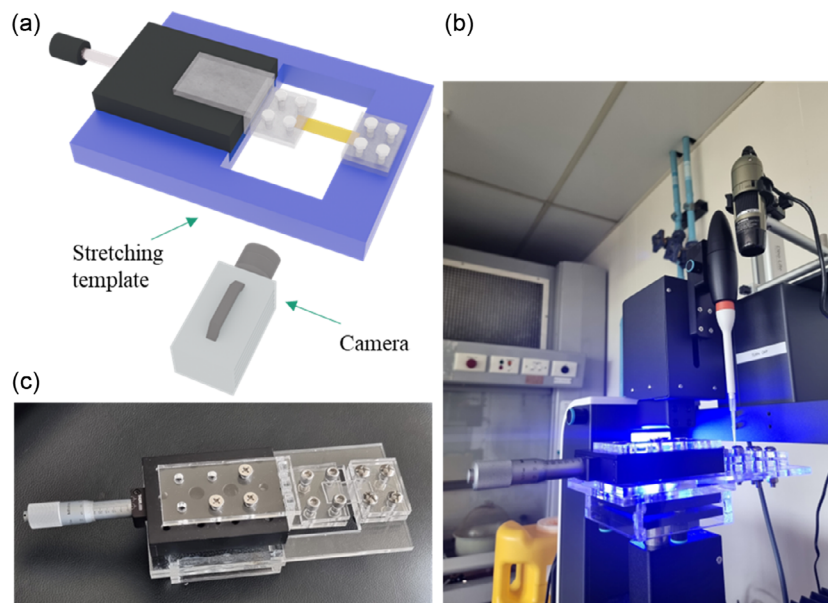


**Figure 2.** Schematic setup of the optical tensiometer and the custom-made stretching platform. a) The illustration of the stretching platform. The green part is made of PMMA to fit onto the stage of the optical tensiometer. The precision positioner (black part) is fixed onto the PMMA stage. The grey part is devised using PMMA to firmly hold the PDMS sample. b) The setup is placed on the stage of the Thetaflex Optical Tensiometer, and the PDMS sample is mounted between the two clamps and stretched using the customized micrometre translation stage. A liquid droplet is placed onto the surface automatically using a controlled dispenser. c) The actual design of the stretching platform.

## 2.4. Surface-Free Energy Measurement

SFE, i.e., surface tension of the solid, was calculated from the CA values using the Owens, Wendt, Rabel, and Kaelble (OWRK) method.<sup>[36]</sup> SFE is a fundamental property of a surface and is defined based on their ideal (flat) configuration. SFE is not affected by surface roughness.<sup>[30]</sup> A superhydrophobic surface is heterogeneous and made up of two components, air and a solid, both of which come into contact with wetting liquids. Therefore, even for surfaces that adhere to the Wenzel and Cassie–Baxter models, which are commonly used to characterize wettable and nonwettable surfaces, respectively, it is challenging to establish the corresponding SFE. Accordingly, the term “normalized surface free energy (NSFE)” was defined to address this problem.<sup>[30]</sup> NSFE forecasts how various liquids would interact with actual surfaces. Considering OWRK method and NSFE, the NSFE of micropillar structures can be obtained by calculating the dispersive,  $\gamma_{sv}^{d*}$ , and polar,  $\gamma_{sv}^{p*}$ , components of the microstructured surface, as follows

$$\sqrt{\gamma_{sv}^{d*}} + \sqrt{\gamma_{sv}^{p*}} \sqrt{\frac{\gamma_{lv}^p}{\gamma_{lv}^d}} = \frac{1}{2} \gamma_{lv} (1 + \cos(\theta_a)) \sqrt{\frac{\gamma_{lv}^d}{\gamma_{lv}^p}} \quad (1)$$

where  $\gamma_{lv}^p$  and  $\gamma_{lv}^d$  are, respectively, the polar and dispersive components of surface tension of the test liquids,  $\theta_a$  is the actual CA of the microstructure surfaces. The detailed derivation of this equation is provided in Section S1 of Supplementary Information.

It should be noted that Equation (1) is valid only when the wetting condition is Cassie–Baxter state,<sup>[30]</sup> i.e., liquid droplets do not penetrate into the gaps of micropillars.

Moreover, to calculate the solid SFE using the OWRK method, it is necessary to have at least two liquids with known dispersive and polar components of surface tensions. This is because there are two unknowns involved in the process, namely, the solid/liquid interfacial free energy and the solid SFE.

The chosen liquids need to be nontoxic, easily accessible, nonvolatile, nonreactive nonsurface swelling, and properly studied.<sup>[37]</sup> There are some commonly used liquids for experiments, such as water, diiodomethane, bromonaphthalene, nitromethane, bromobenzene, toluene, n-hexane, and glycerol. Diiodomethane, bromobenzene, nitromethane, and bromonaphthalene are among those that are harmful and should be minimally used. Toluene and n-hexane are nonpolar liquids that are volatile and swell polymeric test surfaces like PDMS. Therefore, we investigated the surface characteristics of the PDMS films by measuring the apparent CAs with water and glycerol. The polar, dispersive, and total surface tension of water are 51.0, 21.8, and 72.8 mN m<sup>−1</sup>, respectively.<sup>[38]</sup> The polar, dispersive, and total surface tension of glycerol are 30, 34, 64 mN m<sup>−1</sup>, respectively.<sup>[39]</sup> These values were then used to calculate the polar and dispersive components of the NSFE of the solid, Equation (1).

Finally, the total NSFE of the micropillar surfaces,  $\gamma_s^{t*}$ , was obtained after calculating the polar and dispersive components of the solid NSFE, as follows

$$\gamma_s^{t*} = \gamma_{sv}^{d*} + \gamma_{sv}^{p*} \quad (2)$$

## 2.5. Characterization of Wettability of Micropillar Surfaces Using the Stretchable Platform

The PDMS micropillar surfaces were mounted on the mechanical stretcher, Figure 2. The whole setup was placed on the stage of the optical tensiometer. The translation stage was manually stretched from 0 to 5 mm and released backward. The stretching degree is characterized by the strain  $\varepsilon = \frac{\text{displacement length}}{\text{sample length}}$ . Stretching a 10-mm PDMS sample by 0, 1, 2, 3, 4, and 5 mm corresponds to strains of 0%, 10%, 20%, 30%, 40%, and 50%, respectively. Subsequently, it was released back to its original form. The CA measurement was performed at 0%, 10%, 20%, 30%, 40%, and 50% stretching and releasing strains. Figure S2 (Supporting Information) depicts representative images of the apparent CAs of water and glycerol droplets on the PDMS surface with a gap length of 10 μm and diameter length of 5 μm under stretching and releasing. We repeated each experiment at least thrice, and the average values of these CAs were used to calculate the NSFE of PDMS surfaces with micropillar arrays.

The quality and uniformity of the as-prepared microstructured PDMS film were characterized by scanning electronic microscopy (SEM).

## 3. Results and Discussions

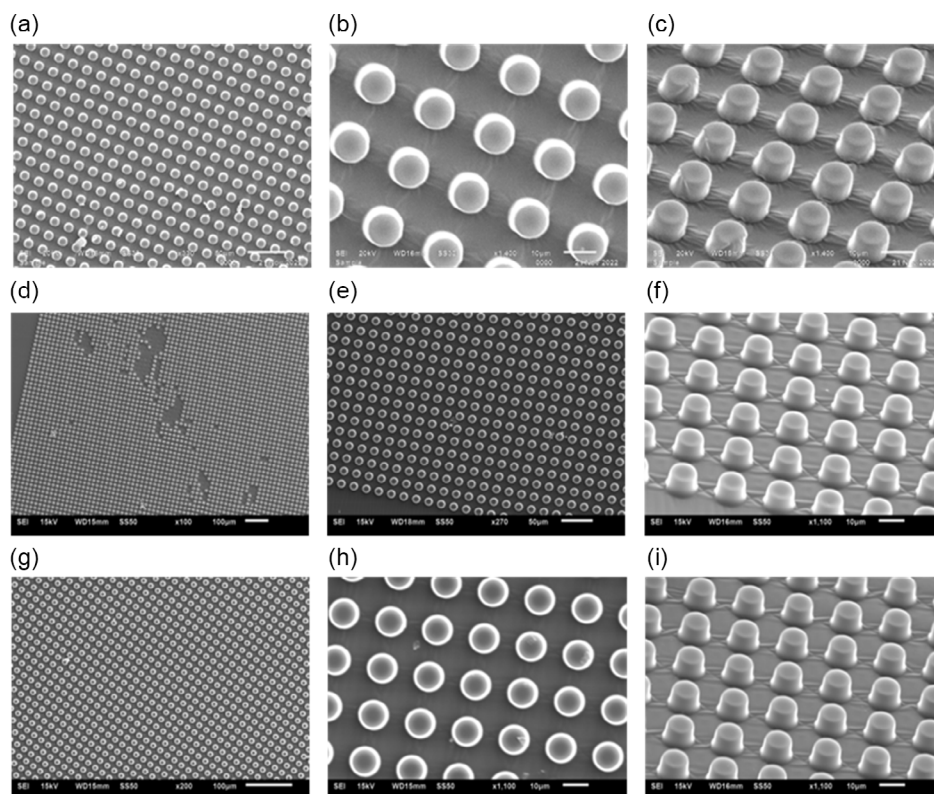
### 3.1. Effect of Stretching on the Dimensions of Micropillar Arrays

Table S1 (Supporting Information) presents the detailed characterization of micropillar dimensions before and after stretching at varying strains. Our findings demonstrate that the fabricated micropillars closely match the intended design with minimal deviation. Although stretching did not significantly alter the diameter of the micropillars at various displacement lengths (data not shown), it caused an increase in the gap between the pillars, approximately 1 μm for every 1 mm displacement. This outcome suggests that stretching tends to expand the gap between micropillars while maintaining the micropillar diameter.

Figure 3a indicates the successful fabrication of PDMS sample with micropillars on top of the surface. Figure 3b,c shows representative scanning electron microscopy (SEM) images with top and side views of the PDMS array created with cylindrical micropillar structures, having a diameter of ≈10 μm, a gap of ≈10 μm, and a height of ≈10 μm. The SEM images in Figure 3b,c indicate that these PDMS arrays are well defined with high accuracy and ordered without defects in large areas.

The results of the stretching experiment on the PDMS surface indicate that the pillars remained intact even after the stretching process. We also took SEM images of the surface area where the clamps are in rigid contact. The result shows that only some minor defects were present, and the PDMS micropillar arrays





**Figure 3.** SEM images of the micropillar array before and after stretching and releasing. a) Representative SEM images of the top section of the fabricated PDMS structures with cylindrical shapes before stretching and releasing. Scale bar: 50 µm. b) Top view of the micropillar array before stretching and releasing at a closer distance. Scale bar: 10 µm. c) Cross-sectional view of the micropillar array before stretching and releasing. Scale bar: 10 µm. d) The top view at a far distance of the micropillar array after stretching where the PDMS surface was in rigid fixation with the two clamps of the stretching platform. The surface shows only some minor defects. Scale bar: 100 µm. e) Magnified view of the micropillar array after stretching where the PDMS surface was in rigid fixation with the two clamps of the stretching platform. Scale bar: 50 µm. f) The cross-sectional view of the micropillar after stretching where the PDMS surface was in rigid fixation with the two clamps of the stretching platform. Scale bar: 10 µm. g) The top view at a far distance of the area where we conduct our experiment after stretching. The PDMS surface shows no defects. Scale bar: 100 µm. h) Magnified view of the micropillar array area after stretching where we conduct our experiment. Scale bar: 10 µm. i) The cross-sectional view of the area where we conduct our experiment after stretching. Scale bar: 10 µm.

showed excellent mechanical stability after the stretching and releasing process. This finding is of great interest as it has implications for the design and development of micro and nanostructures on elastomeric substrates.

Fabricating micro and nanostructures on PDMS surfaces typically involves lithographic techniques, such as soft or nanoimprint lithography. These techniques rely on the use of a master mould that transfers the desired pattern onto the PDMS substrate. However, the challenge with these techniques is ensuring the integrity of fabricated structures during the stretching process. The results presented in this study demonstrate that the pillars on the PDMS surface remained intact after the stretching experiment. This finding suggests that the design and fabrication of micro and nanostructures on PDMS substrates can be optimized to withstand mechanical deformation. Furthermore, the results also have implications for the understanding of PDMS properties. The ability of the PDMS surface to maintain its structure after stretching suggests that the material has a high degree of mechanical stability, which is an important property in micro and nanotechnology applications.

## 3.2. Quantification of Normalized Surface-Free Energy (NSFE)

### 3.2.1. Effect of the Gap and Diameter of Micropillars on NSFE

We calculated the surface energy for each design to analyze the effect of the gap and diameter of micropillars on the characteristics of the surface. We fixed the diameter of the pillars at 10 µm and changed the gap between the pillars accordingly to study the influence of the gap on the NSFE of the sample. Meanwhile, we fixed the gap between pillars at 10 µm and changed the diameter of the pillars accordingly to study the influence of diameter on the NSFE of the sample. We also compared the SFE of flat PDMS with the microstructured PDMS surface. The surface energy of flat PDMS was found to be 12 mN m<sup>-1</sup>. This value agrees well with the surface energy of flat PDMS reported in the literature.<sup>[40]</sup>

It is more significant to take into account the dimensionless values of the parameters related to the pillar. Accordingly, the dimensionless pillar parameter  $D^* = L/G$  is used to denote the relative diameter of the pillars in comparison to their gaps. Table 1 summarizes all the geometrical measurements for these

**Table 1.** Geometric parameters of different pillars fabricated on PDMS substrate (circular pillar, 10  $\mu\text{m}$  height).

$L$ [ $\mu\text{m}$ ]	$G$ [ $\mu\text{m}$ ]	$D^* = L/G$
5	10	0.5
10	10	1
15	10	1.5
20	10	2
10	5	2
10	10	1
10	15	0.67
10	20	0.5

pillar structures. Statistical scattering data of the geometrical parameters are provided in Table S1 (Supporting Information).

We also consider the dimensionless values of the ratio of the NSFE of microstructured PDMS and flat PDMS. The symbol  $\sigma^*$  is used to denote the relative NSFE of microstructured PDMS to that of flat PDMS, i.e.,  $\sigma^* = \frac{\text{NSFE of microstructured PDMS}}{\text{NSFE of flat PDMS}}$ .

Representative images of the apparent CAs on PDMS surface with different diameters and gaps of water and glycerol are shown in Figure S1 (Supporting Information). The results were then used to calculate the NSFE of each surface.

**Figure 4a** shows the variation in the relative NSFE  $\sigma^*$  as a function of dimensionless parameter  $D^*$ . The values of surface energy as the sum of polar energy and dispersion energy were repeatedly calculated three times, and the average values of all the data were reported in the figure. As the  $D^*$  value increases, the relative NSFE,  $\sigma^*$ , decreases. The decrease in relative NSFE implies that as the diameter of the micropillars increases, the equivalent surface tension of the microstructured surfaces decreases. Meanwhile, increasing the gap between pillars increases the relative NSFE. This indicates that by increasing

the gap between pillars, the equivalent surface tension of the microstructured surfaces decreases and becomes closer to that of flat PDMS. When investigating the diameter effect, we kept the gap constant and varied the diameter. Similarly, we kept the diameter fixed and changed the gap to study the gap effect. The result shows a similar trend for both types of experiments. In addition, the result also indicates that the NSFE of our microstructured surfaces was consistently lower than that of flat PDMS. Therefore, the flat PDMS surface has a lower surface tension than the microstructured PDMS surface.

Another interesting point is that the graph in Figure 4a can be divided into two regions. In the first region of  $0 < D^* < 1$ , the trend of diameter and gap effects are similar. This implies that when the diameter of the pillars becomes smaller or the gap between the pillars becomes larger, the NSFE of the microstructured surface reduces in a similar manner. In the second region of  $D^* > 1$ , the red and black lines are moving farther away, indicating a significant difference in diameter and gap effect. We conclude that the size and spacing of the pillars do not have a substantial influence on the way the liquid penetrates and wets the surface. However, even though the ratio of the size and spacing of the pillars can be the same, each dimension can greatly affect how a microstructured surface can repel a liquid and keep the liquid droplets stay on top of the pillars.

Similarly, to analyze the effect of the gap and diameter of micropillars on the wettability of the surface, we measure the apparent CA of each design. We kept the diameter of the pillars constant at 10  $\mu\text{m}$  and varied the gap between pillars to assess the effect of the gap on the sample's wettability. We also kept the gap between pillars constant at 10  $\mu\text{m}$  and altered the diameter of the pillars to evaluate the impact of diameter on the sample's wettability. We measured the apparent CA values three times for each design and calculated the average of all data. Figure 4b depicts the apparent CA variation of the PDMS surface as a function of dimensionless  $D^*$  value. For the diameter effect, the results

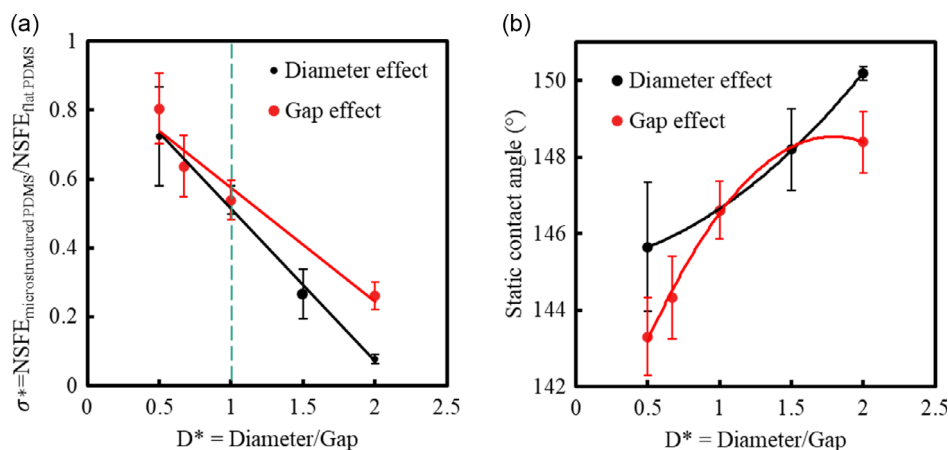


**Figure 4.** a) Variations in the relative surface energy  $\sigma^*$  when changing the dimensionless  $D^*$  value. To investigate the diameter effect, we keep the gap between pillars at 10  $\mu\text{m}$  and vary the diameter of pillars at 5, 10, 15, and 20  $\mu\text{m}$ , respectively (black line). To investigate the gap effect, we keep the diameter of pillars at 10  $\mu\text{m}$  and vary the gap between pillars at 5, 10, 15, and 20  $\mu\text{m}$ , respectively (red line). b) Variations in the water apparent contact angle when changing the dimensionless  $D^*$  value. To investigate the diameter effect, we keep the gap between pillars at 10  $\mu\text{m}$  and vary the diameter of pillars at 5, 10, 15, and 20  $\mu\text{m}$ , respectively (black line). To investigate the gap effect, we keep the diameter of pillars at 10  $\mu\text{m}$  and vary the gap between pillars at 5, 10, 15, and 20  $\mu\text{m}$ , respectively (red line).

showed that increasing  $D^*$  value increases the apparent CA. Meanwhile, for the gap effect, the data revealed that increasing gap between pillars decreases the wettability. These results are consistent with those of the NSFE calculations in Figure 4a. The increasing NSFE decreases the hydrophobicity of the surface, resulting in a decrease in apparent CA. Conversely, a reduction in NSFE leads to an increase in the hydrophobicity of the surface and a corresponding rise in apparent CA.

Based on the current results, we can conclude that our technique can potentially be used to tune the wettability of microstructured surfaces. In the present study, we observed that the wettability of micropillars is affected by factors such as their diameter and spacing. While we have not conducted specific experiments on minimum dimensions, we can extrapolate from our findings that micropillars with smaller dimensions, such as shorter heights and narrower diameters, are likely to exhibit wetting state when subjected to stretching. However, reducing the gap between micropillars can increase the hydrophobicity of the surface. This effect can be attributed to the increased capillary forces and surface tension effects that come into play when the pillars are closer together. As the gap decreases, the meniscus formed by the liquid at the pillar interfaces becomes more pronounced, resulting in a more remarkable alteration in wettability. It is important to note that the exact minimum dimensions for practical wettability tuning may vary depending on the specific material properties and the intended application. Further experimental investigations would be necessary to precisely determine these minimum dimensions. Nevertheless, our current results suggest that micropillars with smaller dimensions hold promise for significant wettability control with stretching.

### 3.2.2. Effect of Stretching and Releasing of Micropillars on NSFE

Figure 5 shows the changes in the NSFE for each design as a function of the strain when the PDMS micropillars with fixed gap length were stretched and then released from 0% to 50% and vice versa. For all four designs, when the PDMS was stretched increasingly from 0% to 50%, the NSFE increased significantly, implying that the hydrophobicity decreased greatly. The opposite trend occurred when we released the PDMS sample. As the strain decreased, the SFE decreased. The NSFE of the stretching process was slightly higher than that of the releasing process, but the difference was not noticeable. The result indicates that the NSFE remained unchanged after stretching and releasing.

Figure 6 illustrates the variations in NSFE for each design in response to the strain when a PDMS sample of fixed diameter length was subjected to stretching and release from 0% to 50% and vice versa. Our results indicate that the NSFE increased significantly, indicating a decrease in hydrophobicity, as the PDMS was stretched from 0% to 50% for all four designs. Conversely, as the PDMS sample was released, the NSFE decreased with decreasing strain. The overall changes in NSFE during the stretching and releasing cycles were not statistically significant, indicating that the NSFE remained unchanged after the stretching and release cycles.

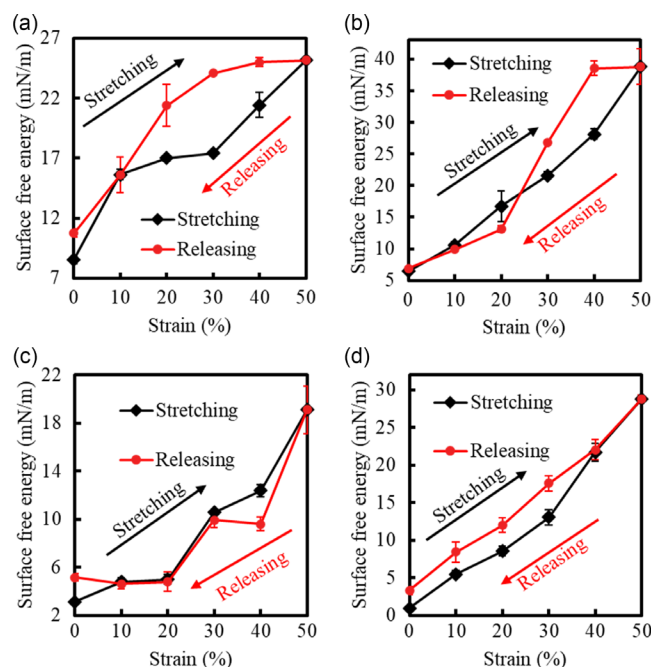


**Figure 5.** Variations in the NSFE when stretching and releasing 0%, 10%, 20%, 30%, 40%, and 50% of the PDMS micropillars with a fixed gap of 10  $\mu\text{m}$ . a) The graph of NSFE versus strain of PDMS sample with micropillars dimension of 5  $\mu\text{m}$  in diameter. b) The graph of NSFE versus strain of PDMS sample with micropillars dimension of 10  $\mu\text{m}$  in diameter. c) The graph of NSFE versus strain of PDMS sample with micropillars dimension of 15  $\mu\text{m}$  in diameter. d) The graph of NSFE versus strain of PDMS sample with micropillars dimension of 20  $\mu\text{m}$  in diameter.

### 3.3. Measurement of Apparent Contact Angles

Figure 7 presents the variations in water CA as a function of strain for each design when the PDMS sample with fixed gap length was stretched and released from 0% to 50% and then released to 0% in similar steps. Our findings demonstrate that for all four designs, as the PDMS was stretched from 0% to 50%, the apparent CA significantly decreased, indicating a substantial decrease in hydrophobicity. Conversely, as the PDMS sample was released, the apparent CA increased with decreasing strain. The wettability of the stretching and releasing processes was found to be similar, suggesting that the wettability of the sample remained unchanged after the stretching and releasing cycles. The results of apparent CA are consistent with the above results of the NSFE.

In Figure 8, we demonstrate the effect of the strain on the apparent CA of each design for the PDMS sample with a fixed diameter length during stretching and releasing from 0% to 50% and vice versa. Our findings indicate that when the PDMS was stretched from 0% to 50%, the apparent CA significantly increased for all four designs, indicating a considerable decrease in hydrophobicity. Conversely, as the PDMS sample was released, the apparent CA decreased with decreasing strain. The wettability of the stretching and releasing process did not show any significant difference, suggesting that the wettability remained unchanged after the stretching and releasing cycles.



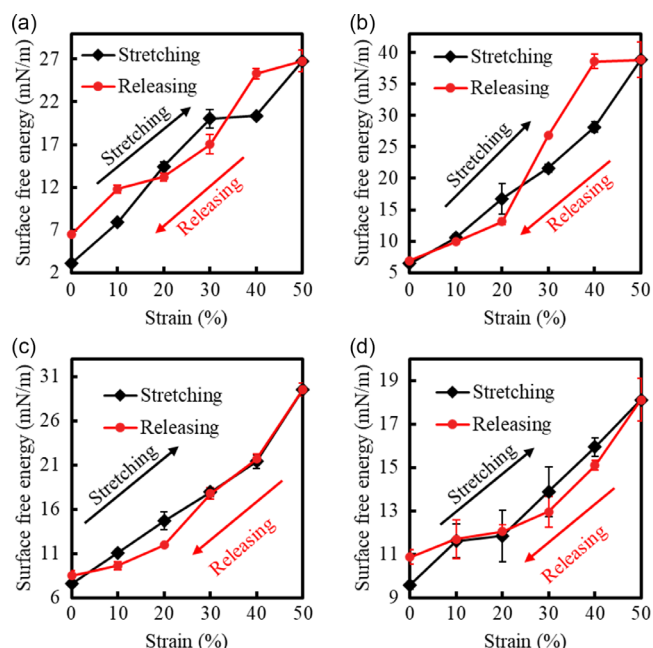


**Figure 6.** Variations in the NSFE when stretching and releasing 0%, 10%, 20%, 30%, 40%, and 50% of the PDMS micropillars with a fixed diameter length (10 μm in diameter). a) The graph of NSFE versus strain of PDMS sample with micropillars with a gap of 5 μm. b) The graph of NSFE versus strain of PDMS sample with micropillars a gap of 10 μm. c) The graph of NSFE versus strain of PDMS sample with micropillars a gap of 15 μm. d) The graph of NSFE versus strain of PDMS sample with micropillars a gap of 20 μm.

## 4. Conclusions

This study demonstrated that the wettability of microstructured surfaces could be tuned reversibly by stretching and releasing cycles. More importantly, to better quantify the wettability of these stretchable microstructured surfaces, the values of NSFE of these surfaces were quantified as a function of both surface topography (diameter and gap of the micropillars) and strain. Comparatively, the obtained NSFE values of all the PDMS microstructured surfaces were less than that of flat PDMS. To investigate the effect of surface topography on the NSFE, the variations of NSFE of microstructured surfaces were obtained as a function of the dimensionless diameter of the pillars,  $D^*$ . It was found that as  $D^*$  of the pillar decreases, the NSFE of PDMS microstructured surfaces becomes closer to that of flat PDMS. Interestingly, we observed that when  $D^*$  was larger than unity, the effect of changing the diameter of micropillars on the variation of NSFE was more pronounced than that of the gaps.

Next, the microstructured surfaces were subjected to stretching and release from 0% to 50% and vice versa, and the variations in NSFE for each micropillar surface in response to the strain were thoroughly quantified. It was observed that stretching could significantly change the values of NSFE. For instance, in the case of the microstructured surface with pillar and gap dimensions of 10 μm, the corresponding NSFE increased from 5 to over 35 mN m<sup>-1</sup> when the surface was stretched from 0% to 50%. Interestingly, the results were reversible by releasing the surface

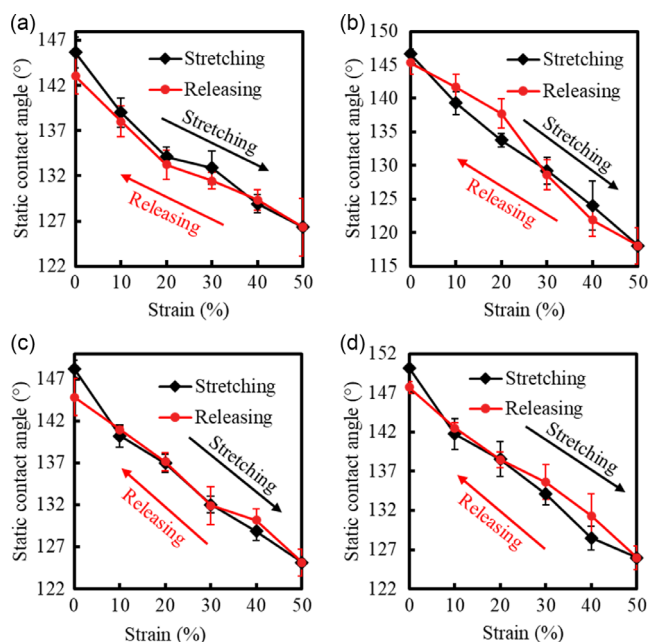


**Figure 7.** Variations in the water apparent contact angle when stretching and releasing 0%, 10%, 20%, 30%, 40%, and 50% of the PDMS micropillars with a fixed gap of 10 μm. a) The graph of apparent contact angle versus strain of PDMS sample with micropillars dimension of 5 μm in diameter. b) The graph of apparent contact angle versus strain of PDMS sample with micropillars dimension of 10 μm in diameter. c) The graph of apparent contact angle versus strain of PDMS sample with micropillars dimension of 15 μm in diameter. d) The graph of apparent contact angle versus strain of PDMS sample with micropillars dimension of 20 μm in diameter.

to its original deformation. All these results agree well with the variations of apparent CAs as a function of both pillar dimensions and strain.

Assessing the limitations of our wettability tuning technique provides a better understanding of the scope and potential applications. The key limitations are as follows:

**Material variation:** The success of our technique might vary based on the material used. Various materials could react in diverse ways to identical treatment. It is important to acknowledge that although our approach could be effective for certain materials, its ability to be used with a wide array of substances might have some constraints.

**Size limitations:** The size and dimensions of the surface features, such as micropillars, may affect the degree of wettability tuning achievable. There may be practical limitations regarding how small or large these features can be for our technique to be effective.

**Surface durability:** The long-term durability of the modified wettability may be a concern. External factors such as wear and tear, exposure to harsh environments, or repeated use could potentially diminish the effectiveness of the tuning over time.

**Fabrication complexity:** Fabricating surfaces with precisely controlled features, such as micropillars, can be technically challenging and costly. The scalability of our technique for large-scale applications might have certain restrictions.



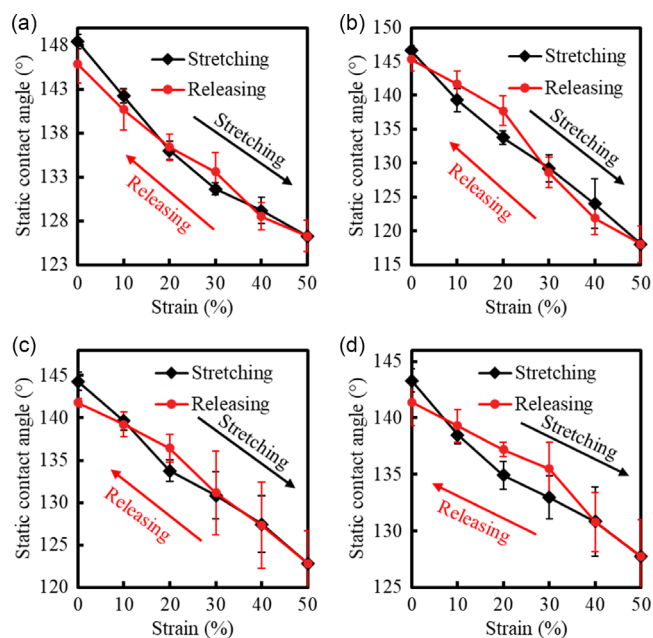


**Figure 8.** Variations in the water apparent contact angle when stretching and releasing 0%, 10%, 20%, 30%, 40%, and 50% of the PDMS micropillars with a fixed diameter length (10  $\mu\text{m}$  in diameter). a) The graph of apparent contact angle versus strain of PDMS sample with micropillars with a gap of 5  $\mu\text{m}$ . b) The graph of apparent contact angle versus strain of PDMS sample with micropillars with a gap of 10  $\mu\text{m}$ . c) The graph of apparent contact angle versus strain of PDMS sample with micropillars with a gap of 15  $\mu\text{m}$ . d) The graph of apparent contact angle versus strain of PDMS sample with micropillars with a gap of 20  $\mu\text{m}$ .

**Environmental effects:** Depending on the chemicals or processes used in the suggested technique, there could be environmental and safety considerations. It would be necessary to assess and deal with any possible environmental consequences.

By recognizing and discussing these limitations, we aim to provide a transparent assessment of the boundaries and considerations associated with our wettability tuning technique. Further research and experimentation, as well as a case-specific evaluation, will be vital for a more detailed understanding of its practical applicability.

Finally, the results of the stretching experiment on the PDMS surface provide valuable insights into the material's mechanical properties and its ability to withstand deformation. This finding has important implications for designing and fabricating micro and nanostructures on elastic substrates. It opens new avenues for developing advanced microfluidic devices and other applications such as wearable biosensors, soft robotics, and energy harvesting devices.

## Supporting Information

Supporting Information is available from the Wiley Online Library or from the author.

## Acknowledgements

This work was performed in part at the Queensland node of the Australian National Fabrication Facility (ANFF). A company established under the National Collaborative Research Infrastructure Strategy (NCRIS) to provide nano and microfabrication facilities for Australia's researchers.

N.K. acknowledges funding support from the Australian Research Council (ARC) Discovery Early Career Research Award (DECRA) DE220100205. N.-T.N. acknowledges funding support from the ARC Discovery Project DP220100261. H.H.V. acknowledges the support from ANFF for the fabrication process.

Open access publishing facilitated by Griffith University, as part of the Wiley - Griffith University agreement via the Council of Australian University Librarians.

## Conflict of Interest

The authors declare no conflict of interest.

## Data Availability Statement

The data that support the findings of this study are available on request from the corresponding author. The data are not publicly available due to privacy or ethical restrictions.

## Keywords

micro/nanofabrication, micropillar surfaces, stretchable microstructures, superhydrophobic surfaces, surface-free energy, tunable wettability

Received: May 30, 2023

Revised: September 1, 2023

Published online:

- [1] D. Patel, V. Jain, J. Ramkumar, *Proc. Inst. Mech. Eng. B: J. Eng. Manufact.* **2018**, 232, 941.
- [2] a) R. Fürstner, W. Barthlott, C. Neinhuis, P. Walzel, *Langmuir* **2005**, 21, 956; b) G. Ciasca, M. Papi, L. Businaro, G. Campi, M. Ortolani, V. Palmieri, A. Cedola, A. De Ninno, A. Gerardino, G. Maulucci, *Bioinspir. Biomim.* **2016**, 11, 011001; c) J.-H. Lee, S. K. Kim, H.-H. Park, T. S. Kim, *J. Micromech. Microeng.* **2015**, 25, 035032; d) N. Kashaninejad, N.-T. Nguyen, W. K. Chan, *Phys. Fluids* **2012**, 24, 112004.
- [3] H. H. Vu, N. T. Nguyen, N. Kashaninejad, *Adv. Mater. Technol.* **2023**, 8, 2370023.
- [4] a) F. Ma, W. Li, A. Liu, Z. Yu, M. Ruan, W. Feng, H. Chen, Y. Chen, *Mater. Res. Express* **2017**, 4, 092001; b) Y. Chen, B. He, J. Lee, N. A. Patankar, *J. Colloid Interface Sci.* **2005**, 281, 458.
- [5] V. Jokinen, M. Leinikka, S. Franssila, *Adv. Mater.* **2009**, 21, 4835.
- [6] B. Xin, J. Hao, *Chem. Soc. Rev.* **2010**, 39, 769.
- [7] a) R. Wang, K. Hashimoto, A. Fujishima, M. Chikuni, E. Kojima, A. Kitamura, M. Shimohigoshi, T. Watanabe, *Nature* **1997**, 388, 431; b) Z. Z. Gu, A. Fujishima, O. Sato, *Angew. Chem.* **2002**, 114, 2171; c) X. Feng, J. Zhai, L. Jiang, *Angew. Chem., Int. Ed.* **2005**, 44, 5115.
- [8] S. Deng, J. Huang, Z. Chen, Y. Lai, *Adv. Mater. Interfaces* **2017**, 4, 1700268.
- [9] T. Sun, G. Wang, L. Feng, B. Liu, Y. Ma, L. Jiang, D. Zhu, *Angew. Chem., Int. Ed.* **2004**, 43, 357.

- [10] E. Bormashenko, V. Multanen, G. Chaniel, R. Grynyov, E. Shulzinger, R. Pogreb, G. Whyman, *Colloids Surf. A: Physicochem. Eng. Asp.* **2015**, 487, 162.
- [11] C. Jia, Q. Wang, P. Chen, S. Lu, R. Ren, *Int. J. Adhes. Adhes.* **2017**, 74, 123.
- [12] T. Li, J. Li, H. Lin, Y. Duan, Y. Xia, Y. Jiang, H. Li, *Appl. Surf. Sci.* **2019**, 473, 393.
- [13] a) Y. M. Hassan, B. H. Guan, L. K. Chuan, A. Halilu, M. Adil, A. A. Adam, B. A. Abdulkadir, *J. Pet. Sci. Eng.* **2022**, 211, 110184; b) Y. Li, J. Li, L. Liu, Y. Yan, Q. Zhang, N. Zhang, L. He, Y. Liu, X. Zhang, D. Tian, *Adv. Sci.* **2020**, 7, 2000772.
- [14] H. Liu, J. A. Piper, M. Li, *Anal. Chem.* **2021**, 93, 10955.
- [15] M. Coux, C. Clanet, D. Quéré, *Appl. Phys. Lett.* **2017**, 110, 251605.
- [16] a) N. Carpi, M. Piel, *J. Vis. Exp.* **2014**, 83, e51193; b) C. K. Nguyen, H. H. Vu, H. V. Dang, N. N. Nguyen, N. T. Le, N. T. Phan, *RSC Adv.* **2017**, 7, 55756.
- [17] N.-T. Nguyen, *Micromachines* **2020**, 11, 1004.
- [18] Z. Huang, Y. Hao, Y. Li, H. Hu, C. Wang, A. Nomoto, T. Pan, Y. Gu, Y. Chen, T. Zhang, W. Li, Y. Lei, N. Kim, C. Wang, L. Zhang, J. W. Ward, A. Maralani, X. Li, M. F. Durstock, A. Pisano, Y. Lin, S. Xu, *Nat. Electron.* **2018**, 1, 473.
- [19] M. Zarei, G. Lee, S. G. Lee, K. Cho, *Adv. Mater.* **2023**, 35, 2203193.
- [20] N. Kashaninejad, A. Munaz, H. Moghadas, S. Yadav, M. Umer, N.-T. Nguyen, *Chemosensors* **2021**, 9, 83.
- [21] N. Kashaninejad, N.-T. Nguyen, *Lab Chip* **2023**, 23, 913.
- [22] J. Zhang, J. Li, Y. Han, *Macromol. Rapid Commun.* **2004**, 25, 1105.
- [23] J. Zhang, X. Lu, W. Huang, Y. Han, *Macromol. Rapid Commun.* **2005**, 26, 477.
- [24] P.-C. Lin, S. Yang, *Soft Matter* **2009**, 5, 1011.
- [25] W.-K. Lee, W.-B. Jung, S. R. Nagel, T. W. Odom, *Nano Lett.* **2016**, 16, 3774.
- [26] J. Liu, W. Wei, F. Cao, Z. Zeng, K. Qian, H. Chen, F. Zhang, W. Li, *Eur. Polym. J.* **2023**, 191, 112057.
- [27] S. M. Lim, J. Ryu, E.-H. Sohn, S. G. Lee, I. J. Park, J. Hong, H. S. Kang, *ACS Appl. Mater. Interfaces* **2022**, 14, 10825.
- [28] V. M. Villapun Puzas, L. N. Carter, C. Schröder, P. E. Colavita, D. A. Hoey, M. A. Webber, O. Addison, D. E. T. Shepherd, M. M. Attallah, L. M. Grover, S. C. Cox, *ACS Biomater. Sci. Eng.* **2022**, 8, 4311.
- [29] S. Laurén, [White Paper] Biolin Scientific **2022**, <https://www.biolinscientific.com/hubfs/Content%20Offer/Attension/EN/AT%20WP%203D%20Topography%202020.pdf?hsLang=en>.
- [30] M. Shaker, E. Salahinejad, *Prog. Org. Coat.* **2018**, 119, 123.
- [31] L. Amato, S. S. Keller, A. Heiskanen, M. Dimaki, J. Emnéus, A. Boisen, M. Tenje, *Microelectron. Eng.* **2012**, 98, 483.
- [32] N. Kashaninejad, W. K. Chan, N.-T. Nguyen, *Langmuir* **2012**, 28, 4793.
- [33] S. Misra, Y. Jin, *Multifrequency Electromagnetic Data Interpretation for Subsurface Characterization*, Elsevier, Netherlands **2021**, p. 145.
- [34] J. Bostwick, P. Steen, *J. Fluid Mech.* **2014**, 760, 5.
- [35] S. Li, M. Liu, D. Hanaor, Y. Gan, *Transp. Porous Media* **2018**, 125, 193.
- [36] a) M. Annamalai, K. Gopinadhan, S. A. Han, S. Saha, H. J. Park, E. B. Cho, B. Kumar, A. Patra, S.-W. Kim, T. Venkatesan, *Nanoscale* **2016**, 8, 5764; b) D. K. Owens, R. Wendt, *J. Appl. Polym. Sci.* **1969**, 13, 1741; c) D. Kaelble, *J. Adhes.* **1970**, 2, 66.
- [37] Z. Zhang, W. Wang, A. N. Korpacz, C. R. Dufour, Z. J. Weiland, C. R. Lambert, M. T. Timko, *Langmuir* **2019**, 35, 12317.
- [38] E. Rynkowska, K. Fatyeyeva, S. Marais, J. Kujawa, W. Kujawski, *Polymers* **2019**, 11, 1799.
- [39] J. Ou, G. Zhao, F. Wang, W. Li, S. Lei, X. Fang, A. R. Siddiqui, Y. Xia, A. Amirfazli, *ACS Omega* **2021**, 6, 7266.
- [40] Y. G. Kim, N. Lim, J. Kim, C. Kim, J. Lee, K.-H. Kwon, *Appl. Surf. Sci.* **2019**, 477, 198.